Journal of Dynamic Behavior of Materials (2020) 6:246–265
https://doi.org/10.1007/s40870-020-00241-z

RESEARCH PAPER

Dynamic Flow Stress Behavior of Hypo-Eutectoid Ferrite-Pearlite Steels Under Rapid Heating

S. P. Mates[1] · E. Vax[2] · R. R. Rhorer[3] · M. R. Stoudt[1]

Received: 20 May 2019 / Revised: 4 February 2020 / Accepted: 4 March 2020 / Published online: 14 April 2020

Abstract

In the machining process, the workpiece undergoes large plastic deformation at high strain rate and is heated rapidly by plastic work and friction. Rapid temperature excursions brought about during this process may result in non-typical microstructures whose mechanical behavior differs from what has traditionally been observed and modeled. This paper presents dynamic stress-strain measurements on three hypo-eutectoid ferrite-pearlite carbon steels of increasing carbon content (AISI 1018, 1045 and 1075) under rapidly heated conditions, with total heating times less under 4 s, up to 1000 °C. The mechanical behavior of these steels is broken down into four regions: low temperature thermal softening, followed by dynamic strain aging, pearlite decomposition and, finally, ferrite-austenite thermal softening. The present rapidly heated high strain rate results are generally commensurate with literature data up through dynamic strain aging to about 700 °C, indicating limited effects of short heating times below the pearlite decomposition temperature (A1). Above A1, however, the results diverge significantly, owing to the limited time for diffusion processes that govern the transformation from ferrite-pearlite to ferrite-austenite and finally austenite. The divergence includes an inversion of the effect of carbon content on flow stress above A1 compared to previous studies with longer heating times.

Keywords Kolsky bar · Machining · Steel · High strain rate · High heating rate

Introduction

Simulations of machining processes are not fully successful to date, which represents a barrier to realizing optimal material removal rates, energy efficiency and tool life [1, 2]. A recent review of the field calls attention to the lack of consistent and reliable material models that are applicable to machining conditions [3]. These conditions, which can involve strain rates up to 10^6 s^{-1}, temperatures up to 1000 °C and heating rates exceeding 1000 °C/s, are beyond most laboratory testing techniques. This, along with the fact that machining creates a more complex stress state than uniaxial material testing and also involves significant friction effects, has motivated efforts to extract material properties by applying inverse methods to instrumented machining experiments, using both analytical [4] and numerical modeling [5–9]. Carbon steel behavior is particularly complex compared to other materials. One important effect included in sophisticated machining models of ferrite-pearlite steels is dynamic strain aging (DSA), referred to as "blue brittleness" in the machining literature, where the steel becomes stronger and less ductile under certain conditions of temperature and strain rate [7, 10]. Another important effect is the austenite transformation on heating, which when followed by rapid cooling of the chips and workpiece surface results in complex mixed microstructures consisting of ferrite-pearlite, bainite and/or martensite [11]. The "white layer" observed on the machined surfaces of high strength steels is attributed to rapid cooling of a surface austenite layer formed during machining [12]. Dynamic recrystallization is another effect that is suspected to influence the grain size and surface hardness in cold or dry machining in some steels [3]. It has also been observed in chips at moderate cutting velocities when machining strong martensitic steels [13]. Such complex

✉ S. P. Mates
steven.mates@nist.gov

[1] National Institute of Standards and Technology, 100 Bureau Drive, Gaithersburg, MD, USA

[2] Nuclear Research Center Negev, Negev Desert, Israel

[3] Rhorer Precision Engineering LLC, 118 Summit Hall Rd, Gaithersburg, MD, USA

metallurgical effects are often diffusion-related and thus depend on time as well as temperature.

Temperature effects on the dynamic flow stress of carbon steel were first investigated by Manjoine [14] using a rotating flywheel experiment to study mild steel in tension at temperatures up to 600 °C at a strain rate of 200 s^{-1}. Significant dynamic strain aging (DSA) effects were identified, causing an increase in the plastic flow stress between 400 and 600 °C. Campbell and Ferguson [15] examined temperature effects on yield strength in a 0.12% C[1] steel using a double shear specimen at strain rates up to 40,000 s^{-1} and temperatures to 440 °C. They did not observe DSA, however, perhaps because of the limited plastic strain in their tests. The dynamic compression behavior of carbon steel was studied by Oyane et al. [16] covering steels from 0.16 to 0.52% C and temperatures up to 1000 °C at a strain rate of 450 s^{-1}, and the extensive data set was reported in Oxley's classic machining text [4]. The results showed prominent DSA effects that were manifest as a bell-shaped region of elevated flow stresses between about 400 and 800 °C, where the latter temperature exceeded the austenite transformation temperature. Shirakashi et al. [17] developed a rapid induction heating method and combined it with a compression Kolsky bar technique to study a 0.18% carbon steel at strain rates up to 2000 s^{-1} and temperatures up to 800 °C with heating times limited to 5 s. Their results agreed with the earlier data of Oyane et al. [16], and they further explored possible time-dependence of DSA and austenite transformation. They found no significant modification of DSA behavior with heating time, exploring with a separate method heating times down to 40 ms. Shirakashi et al. [17] further explored austenite transformation via rapid heating and quenching followed by hardness testing and concluded that the heating time required to transform steel exceeded 1 ms even when heated above A3. They concluded transformation could not occur during machining, where the heat time was significantly lower than 1 ms. Later, an induction heating technique was employed by Jaspers and Dautzenberg [18] on a 0.45% C steel in high strain rate compression tests up to 600 °C. This data also shows some thermal hardening, apparently due to DSA, but both the onset temperature and the magnitude of the effect were different from earlier literature data. Lee and Liu [19] used a radiation furnace arrangement with a Kolsky bar to study a low, medium and a high carbon steel up to 800 °C with a maximum strain rate of 5500 s^{-1} to a large plastic strain, but their experimental results showed neither DSA or phase transformation effects. Aside from the data provided but Oxley [4] and Lee and Liu [19], high-strain-rate, high-temperature data sets for carbon steels have been restricted to a single composition, so that effects of carbon content remain not well studied. The Oxley data set [4] has seemingly not received attention outside of the machining science community, and that of Lee and Liu [19] does not reflect the strong DSA effects of the most other comparable data sets. Aside from the pioneering work of Shirakashi et al. [17], the effect of heating time on dynamic plasticity in carbon steels has not been explored.

The foregoing work on steel plasticity suggests that the primary influence of heating time involves the phase transformation to austenite from the initial ferrite-cementite microstructure. This transformation radically alters the environment of obstacles through which dislocations are driven [20]. Further, as the primary crystal structure changes from body centered cubic (BCC) ferrite to face centered cubic (FCC) austenite, DSA effects will also likely change. Dynamic strain aging is most notable in BCC steels and involves the development of a Cottrell atmosphere of solute atoms around dislocation cores that act to pin them until higher stresses are applied to move them again [21]. In carbon steels, the atmosphere involves interstitial carbon and nitrogen, and is responsible for so-called "jerky" or "serrated" stress–strain behavior and a significant increase in the hardening rate for specific ranges of strain rate and temperature that can result in negative strain rate sensitivity and lower ductility [22]. Later work on DSA in carbon steels has indicated an influence of Mn content [23] under low-rate deformation, and the effects of other microstructural features such as grain size and prior cold work have been reviewed [24]. So-called "killed" steels, which are processed to achieve exceptionally low oxygen levels, exhibit much less DSA than ordinary carbon steels [25, 26]. Such steels are used commercially in the auto industry for applications requiring high formability, and generally have very low carbon content. However, thermal hardening can still occur in these steels at high strain rates, and the effect is enhanced by prior cold work making DSA potentially time-sensitive above recovery temperatures [27]. Interestingly, although dynamic strain aging also occurs in FCC materials in the form of serrated stress–strain behavior, the strong increase in hardening does not seem to occur or is less-pronounced [22]. DSA-enhanced hardening can occur in FCC alloys, but most of these studies involve austenitic stainless steels [28] and not plain carbon steels above austenite formation temperatures. Thus, when a carbon steel transforms from ferrite-pearlite to austenite under rapid heating and high strain rate loading, dynamic strain aging effects may change considerably.

The influence of heating rate and time on austenite transformation in ferrite-pearlite steels has been well studied, primarily in connection with steel processing research but also in connection with welding research, where weld microstructure and properties depend critically on the rapid thermal excursions taking place. Cementite (Fe_3C), the primary

[1] All composition information is reported as mass percent.

strengthening precipitate in plain carbon steel, becomes unstable above the A1 temperature, usually between 700 and 730 °C, depending on the steel composition. Pearlite colonies, which consist of alternating plates of cementite and ferrite (BCC iron), decompose into austenite (FCC iron) which has high carbon solubility. The growth of austenite begins first within pearlite colonies and, once they are rapidly consumed, a second stage of slower growth occurs as the austenite grains consume the remaining globular ferrite, eventually homogenizing the carbon distribution through the microstructure [29–31]. Under welding conditions, pearlite is considered to dissolve almost instantaneously [32]. Studies of austenite growth in pure pearlite (eutectoid steel composition) under isothermal conditions and continuous heating have shown dissolution times can be on the order of seconds [33] up to a few minutes [34] depending on temperature and the cementite plate thickness and pearlite colony size. Transformation kinetics slow down when these two features coarsen [33–35], but they increase with temperature and heating rate. The quantity Mn and Si have also been shown to affect the observed transformation rate [29, 36]. Under extremely fast heating, austenite growth behavior may change substantially [37, 38]. Two main heating techniques have been used to study pearlite dissolution kinetics: liquid immersion, in which the sample is immersed in a fixed-temperature bath [34], or external heating via radiative [33], inductive [31] or resistive [39] methods. For the external heating methods, temperature gradients within the sample are essentially unavoidable due to radiative and possibly convective heat loss to the colder surroundings [40], although efforts are made to limit this issue with radiation shielding and specialized sample geometries. For steels near A1, thermal gradients will bias transformation kinetics data. Measurements by the present authors on the kinetics of pearlite decomposition indicated significant transformation occurs in under three seconds for the steels studied here, but the transformation is not uniform due to thermal gradients in the specimens [39]. Despite the variance in the timescales for pearlite decomposition determined from different studies and the experimental difficulties associated with measuring them, heating times in machining are well below one second, making it rather likely that carbon steel deviates significantly from normal flow stress behavior if cutting temperatures exceed A1.

Between the A1 temperature and the temperature at which carbon steel becomes fully austenitic (called A3), steel exists as a two-phase mixture of BCC ferrite with low carbon content and FCC austenite with high carbon content. The A3 temperature increases significantly with decreasing carbon content, reaching 910 °C for fairly pure iron [41]. Carbon homogenization is governed by bulk diffusion of carbon through austenite grains and occurs over timescales much larger than those associated with pearlite decomposition. As a result, within the A1 to A3 temperature window (called the intercritical region) and perhaps beyond, the plastic behavior of carbon steel will deviate significantly from equilibrium under rapid heating conditions. Studies of steel plasticity above the A1 temperature have been performed to design optimal hot rolling procedures by examining the effects of time, temperature and composition effects on rolling stresses and on the final microstructure and properties of rolled steel products. Hatta et al. [42] developed a model for carbon steels of various carbon contents and strain rates up to 100 s^{-1} and temperatures up to 1000 °C with extensive comparison to literature data obtained under conventional heating conditions. In the model, equilibrium thermodynamics is used to determine the phase fractions in the intercritical region, and so it is assumed to represent equilibrium mechanical behavior of steel in this region. As such, this model serves as a useful guidepost against which rapidly-heated mechanical data can be compared.

A final potential source of time-dependent flow stress behavior is associated with steels in the cold-worked condition, where recovery and recrystallization can occur even at sub-critical temperatures (below A1) [43]. Recovery and recrystallization are sensitive to the amount of Mn, Mo and Cr in the steel. As with carbon diffusion, recovery and recrystallization take place on time scales significantly longer than that associated with cementite decomposition (seconds or less), and as such these effects may cause significant differences in the plastic behavior of steel with extended heating times compared to what occurs under fast heating conditions. Annealing kinetics for cold-rolled low carbon steel show that the strength can fall within 20 s at 600 °C [44]. Earlier work by Shirakashi et al. [17] indicated annealing requires about 90 s in low carbon steel that has been cold worked to a strain of 0.3, which is in rough agreement with the former finding. Cementite plates can also coarsen (spherodize) in the sub-critical region, adding another potential source of time-sensitive mechanical behavior. More recent studies indicate that, under rapid heating, recovery processes do occur but recrystallization may be bypassed [38]. However, as these effects are mostly important in cold-worked steels, their relevance to machining annealed materials is questionable.

To address the need for additional high temperature, high strain rate flow stress for carbon steels under short, controlled heating times, we use an electrically pulse-heated Kolsky bar technique developed at the National Institute of Standards and Technology (NIST) [45] to measure three hypo-eutectoid ferrite-pearlite steels that have been heat treated to obtain similar pearlite morphologies but with three increasing volume fractions of pearlite up to near-eutectoid composition. We note the absence of so-called electro-plasticity effects in this technique [46], which are non-thermal effects sometimes reported during metal deformation tests

performed under large DC currents [47], such that all effects observed are believed to be related only to temperature, time and strain rate. Strain rates range between 2000 and 5000 s^{-1}, depending on specimen geometry and strength, and the behavior is examined up to an average plastic strain of about 0.25. Finally, all the data presented here are obtained using a single heating pulse duration of less than 4 s. An initial study showed that variations in the heating time on the order of seconds can influence carbon steel flow stress above A1 due to phase transformation effects [39]. While the present work does not explicitly explore the effect of variable heating time on flow stress, studies on this topic are ongoing and will be reported in the future.

Experimental

Material Preparation

Tests were conducted on commercial AISI 1018 (ASTM A108) and AISI 1075 (ASTM A684) steels acquired as cold-rolled plate, and AISI 1045 (ASTM A108) steel acquired as cold-drawn rod. Disk-shaped compression specimens, measuring 2 mm thick by 4 mm in diameter from plate or 4.75 mm in diameter from rod, were wire EDM machined from the stock material, then ground flat. The specimen diameter was selected to be much smaller than the Kolsky bar diameter (15 mm) to concentrate resistive heating in the specimen and minimize bar heating. Material compositions, determined by spectrographic analysis (ASTM E1019 and ASTM E415), are listed in Table 1. The 1018 and 1075 steels were heat treated at 820 °C for 45 min and then air-cooled to promote the formation of a fine, pearlitic microstructure. The 1045 steel was heat treated at 900 °C for 1 h and air cooled to achieve a similar pearlitic structure. Representative microstructures for the three carbon steels, revealed using metallographic preparation with a 2% nital etch, are shown in Fig. 1. Equilibrium thermodynamic calculations of the A1 and A3 temperatures for each composition are listed in Table 2. Ferrite grain size and pearlite colony size were measured from optical micrographs following ASTM-E112, while pearlite interlamellar spacing was measured following the method described by Caballero et al. [33]. These data, along with pearlite volume fractions obtained from point counting, are given in Table 3.

Pulse-Heated Kolsky Bar Method

This method combines a traditional compression Kolsky bar arrangement with rapid resistive heating [45]. The Kolsky bar apparatus consists of maraging steel incident and transmission bars measuring 15 mm in diameter and 1.5 and 1.47 m in length, respectively, the latter being shorter to allow recovery testing. The bars are outfitted with short sacrificial tips (3 cm long) made from hardened maraging steel of the same diameter as the bars. The tips are threaded into the primary bars and can easily be removed and re-ground when damaged by occasional electrical arcing. The primary bars are in an un-hardened condition and have a Young's modulus and wave speed of 170 GPa ± 2 GPa and 4600 m/s ± 25 m/s, respectively. The tests were conducted with a 250 mm long striker impacting at a velocity of 10.0 m/s ± 0.2 m/s. This striker impact produced maximum plastic strains of between 0.15 and 0.5 in our test specimens, depending on the initial temperature and specimen strength. Because of the loss in specimen strength with temperature, true strain rates also increased from 2000 to 5000 s^{-1} for our tests from room temperature to the maximum temperature. Annealed copper pulse shapers measuring 6.35 mm in diameter and 0.254 mm thick were used in all tests to limit wave dispersion in the tests. Finally, the punching correction technique of Safa and Gary [48] was used to compensate for elastic deformation of the bar ends around the small samples.

Heating current is supplied via a bank of six large lead-acid batteries connected in series, with 2 V per cell delivering a maximum of 12 V. Sample temperature is controlled by modulating the current supplied to the sample through adjusting the gate voltage supplied to an array of field effect transistors (FETs) to match the setpoint via a custom proportional-integral-derivative (PID) microcontroller unit (loop time of 0.0001s). Temperature is sensed by an infrared InGaAs spot pyrometer with a peak responsivity at a wavelength of 1.5°μm and an amplifier of bandwidth 800 kHz. The pyrometer views a spot on the sample surface measuring approximately 1 mm^2. For temperatures below 350 °C where the pyrometer becomes insensitive to temperature, a current setpoint is used to control the heating. Current is measured using a standard resistor placed in series in the heating circuit. To facilitate uniform heating and reduce arcing and localized melting, thin graphite foil disks (0.13 mm thick) are placed between the specimen and the bar ends. Although thin, the foils reduce the strain experienced by the specimen, and the effect is compensated for by subtracting the foil contribution to the deformation using an empirical correction formula [45]. Because the heating times are limited to less than 4 s, and because the sample diameter is much smaller than the bars (4 mm versus 15 mm), the heat affected zone in the bars was found to be too small to disturb elastic wave propagation [49].

The uniformity of the sample temperature is monitored using a second infrared pyrometer focused on the opposite side of the specimen from the control pyrometer, as shown in Fig. 2. Tests are accepted only if the two pyrometer signals are in accord with one another over the latter half of the thermal history. The thermodynamic temperature of the sample is measured with a K-type thermocouple (0.127 mm diameter) that is welded to the specimen adjacent to

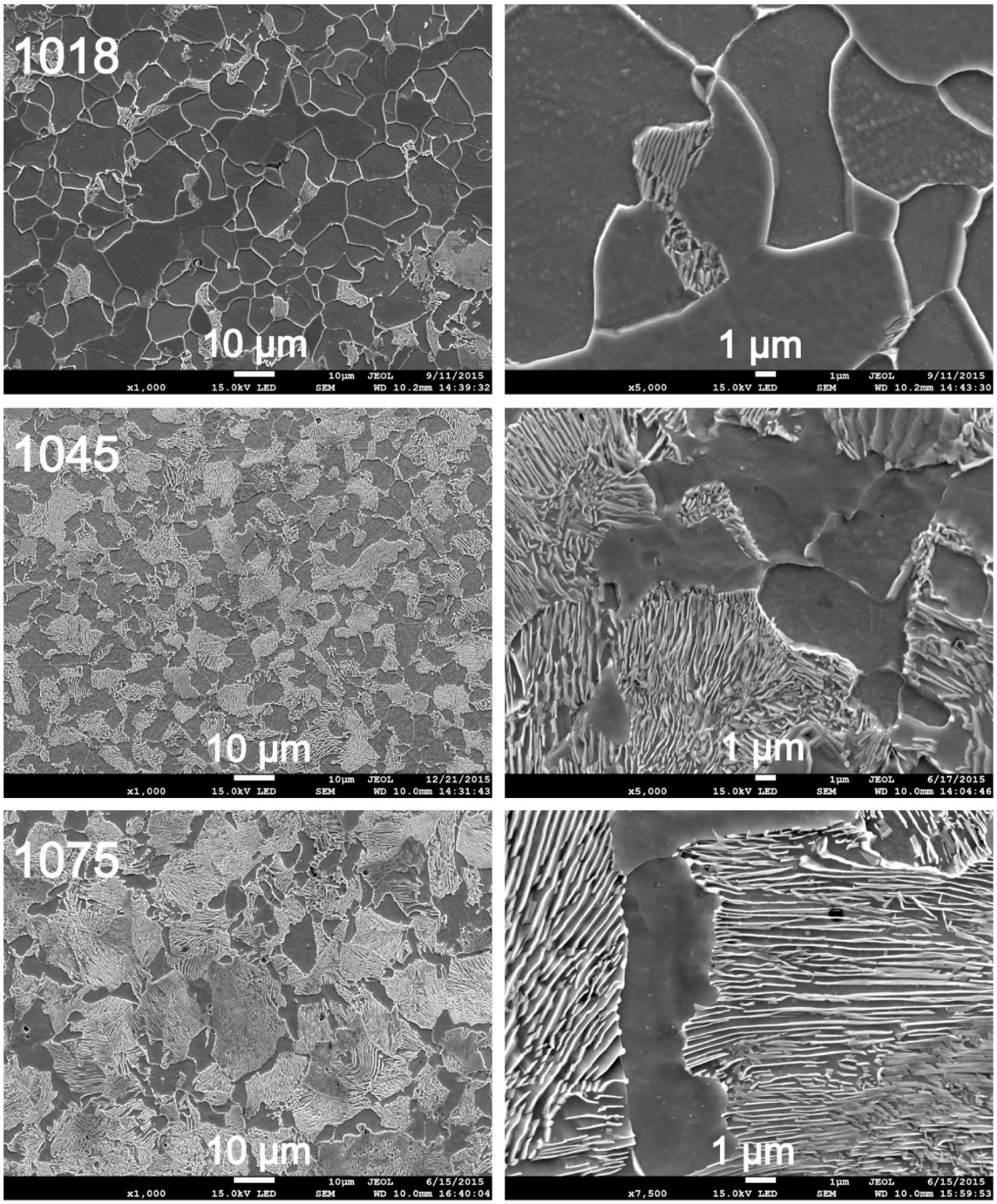

Fig. 1 SEM micrographs of the three carbon steels investigated (2% nital etch)

Table 1 Compositions of steels investigated in weight percent

Designation	C	Mn	P	S	Si	Ni	Cr	Mo	Cu	Method
1018	0.2	0.6	0.009	0.006	0.02	0.08	0.06	0.02	0.14	ASTM E1019/E415
1045	0.48	0.73	0.005	0.007	0.19	0.04	0.08	0.01	0.10	ASTM E1019/E415
1075	0.72	0.6	0.013	< 0.005	0.24	0.05	0.07	0.02	0.11	ASTM E1019/E415

Table 2 Equilibrium thermodynamic calculations of the A1 and A3 temperatures

Designation	A1 [°C]	A3 [°C]
1018	709	836
1045	712	760
1075	717	727

the spot viewed by the control pyrometer. Each wire of the thermocouple is welded individually to the sample surface (separated-junction method [50]), usually in a small region near the spot observed by the control pyrometer. During heating, the thermocouple signal is rendered unreliable by bias and noise from induction from the heating current's electric field, which persists for about 15 ms after the current is switched off. An accurate impact temperature measurement is therefore only possible after the thermocouple signal stabilizes, so the loading pulse is delayed by about 20 ms after current shutoff by triggering the current shutoff on the striker bar velocity signal. Additionally, the sample cooling history can usually be obtained because often the thermocouple remains attached after impact, which is critical for interpreting post-test microstructures in tests where phase transformation occurs. To inhibit oxidation during heating, a vacuum chamber is placed around the ends of the bars and the specimen, as shown in Fig. 3. A low vacuum was also found to improve heating consistency and limit arcing. The control and monitoring pyrometers view the sample through CaF_2 widows that allow high infrared transmittance between 0.25 and 7 µm.

The true thermal history of the specimen is estimated from the pyrometer signal and an effective emissivity, ε, determined from the thermocouple temperature at impact (T) and the pyrometer temperature signal (T_{rad}) using the following [51]:

$$T = \frac{1}{\frac{1}{T_{rad}} + \frac{\lambda \ln(\epsilon)}{c_2}} \quad (1)$$

λ is the effective wavelength of the pyrometers (1200 nm), and c_2 is the second radiation constant, 0.014388 mK. The effective emissivity is plotted as a function of temperature in Fig. 2 all three steels. As this plot shows, the emissivity values are scattered, preventing an a priori assignment of an emissivity value that could be used for all tests. Emissivity can vary for a variety of reasons, including changes in surface quality and surface temperature uniformity from test to test.

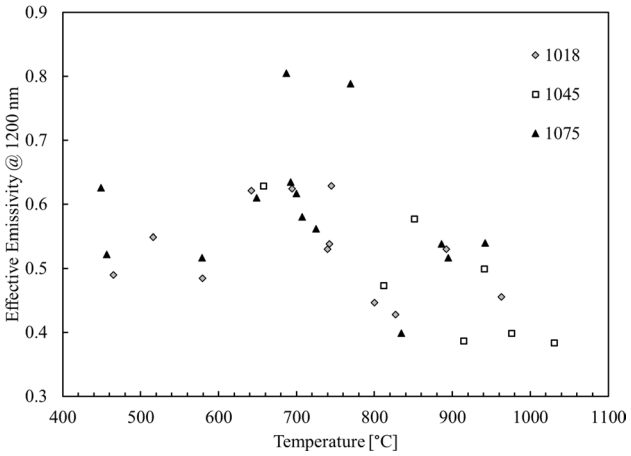

Fig. 2 Effective emissivity determined from pulse heated tests using Eq. 1

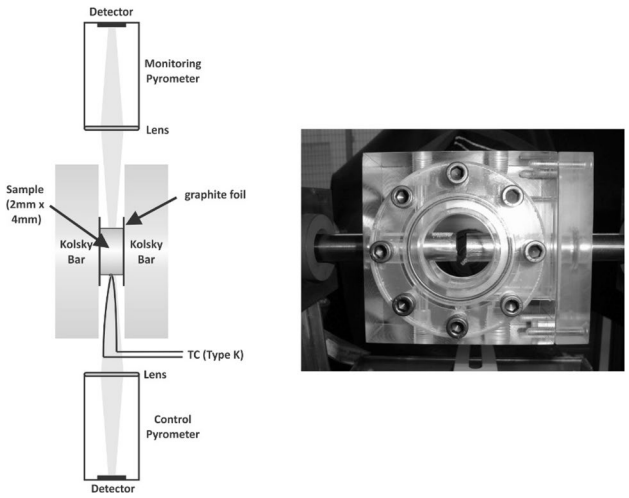

Fig. 3 Thermal measurement setup (left) and vacuum chamber (right)

Table 3 Microstructural measurements of the three carbon steels investigated

Designation	Pearlite volume fraction	Avg. ferrite grain size [µm]	Avg. pearlite colony size [µm]	Avg. inter-lamellar spacing [µm]
1018	0.15 ± 0.03	8.0 ± 1.5	3.9 ± 0.5	0.18 ± 0.02
1045	0.56 ± 0.06	4.2 ± 0.2	4.2 ± 0.2	0.21 ± 0.02
1075	0.77 ± 0.08	n/a	3.0 ± 0.2	0.24 ± 0.02

Uncertainties are 95% CI

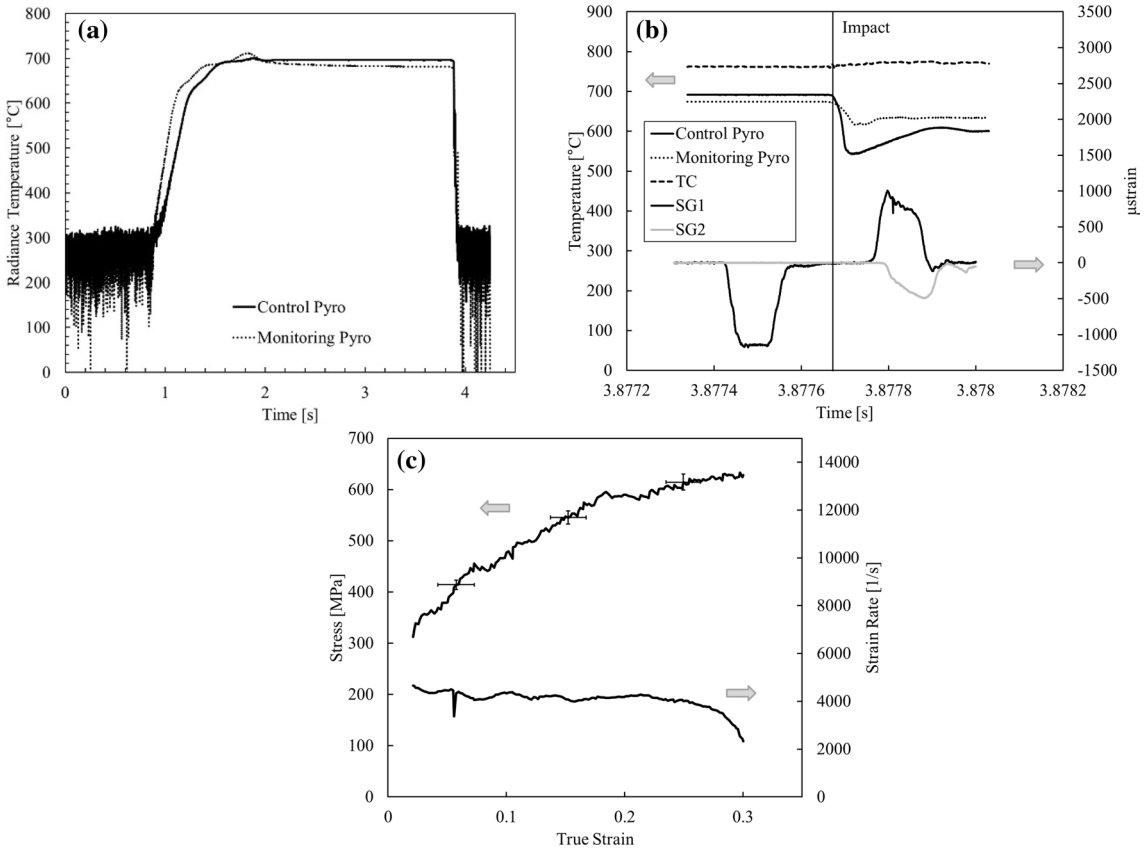

Fig. 4 Typical experimental data set for a single pulse-heated Kolsky bar measurement on 1045 steel at a test temperature of 728 °C ± 40 °C. **a** Radiance temperature history. **b** Kolsky strain waves and temperature signals at impact. **c** True stress–strain and strain rate–strain curves after foil correction

Voltage signals from the two pyrometers, the thermocouple, the FET control voltage and the current sensor are measured at 200 kHz during the heating process. The strain gage signals are measured using the same recorder, but the recording rate is increased to 2 MHz via triggering to fully resolve the strain waves for the mechanical test. Thermocouple data are filtered to 50 kHz to reduce high-frequency noise. All analog voltages are recorded with 14 bit resolution. Foil-type 1000 Ω strain gages are used to measure the strain waves. Two gages are bonded to each bar, and the bridge circuits are completed with identical dummy foil gages mounted to small pieces of identical material for temperature compensation. The bridge circuits are powered by four 6-V alkaline lantern batteries connected in series (24 V total). To adjust for the reduction in bridge excitation voltage as the batteries gradually discharge, the bridge circuit is calibrated every few hours using the parallel resistor method.

Figure 4 shows typical experimental data for a single test, consisting of (a) a thermal history plot, (b) Kolsky bar strain waves and temperature readings at the time of impact, and (c) corrected stress–strain response with estimated uncertainties (c). The thermal history plot indicates the total heating time and approximate temperature uniformity during heating. At impact, plot (b) shows the pyrometer signals as they drop off suddenly when the specimen is moved out of the field of view by the motion of the Kolsky bar. However, the thermocouple survives impact and indicates a slight increase in temperature owing to adiabatic heating effects. Finally, the example stress–strain and strain rate-strain plots are from a test on 1045 steel at 728 °C and at an average strain rate of 4000 s^{-1}, with strong strain hardening and relatively low stress near yield.

Thermal gradients in the sample occur due to very large conductive heat flux into the bars, which for example allows sample cooling rates often in excess of 500 °C/s for samples that remain trapped in the bars after an impact test or in heat-only tests after the heating current is turned off, as shown in Fig. 5 (right). This large conductive heat flux dominates the overall heat transfer from the sample. Cooling data show how samples that are ejected after impact, which happens occasionally, cool ten times slower than trapped specimens (Fig. 5). Radiative and convective heat losses are much smaller than the heat loss into the bars but they are not negligible. Cooling data for ejected samples

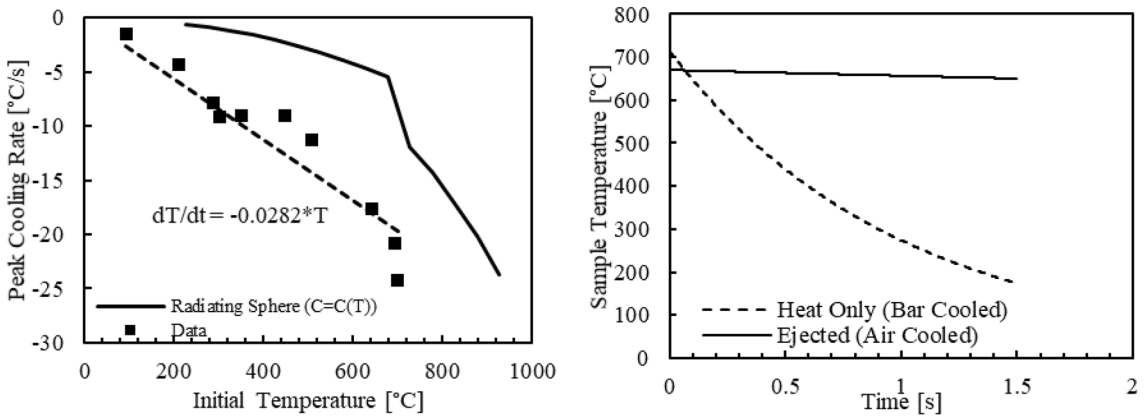

Fig. 5 Peak cooling rate data for specimens ejected on impact compared with radiating sphere model with temperature-dependent heat capacity (C = C(T)) (left), and comparison of cooling data for ejected tests with heat-only tests showing the high cooling rate due to heat flux into the bars

are compared in Fig. 5 to a simple equivalent-sphere radiation model for steel radiating in a vacuum, using an effective graybody emissivity of 0.55 and a variable heat capacity for steel. The cooling data show significantly higher cooling rates than the simple sphere model, which can be explained by differences in the aspect ratio of the body (flattened cylinder versus a sphere) and the possible influence of convection. A simple linear fit to the cooling data is used to determine an effective heat transfer coefficient for the exposed surface to combine both radiative and convective effects using the following model:

$$\frac{dT}{dt} = -\frac{hA_s\left(T - T_\infty\right)}{\rho Vc} \tag{2}$$

In this equation, the T is the sample temperature, t is time, h is the effective heat transfer coefficient, A_s is the surface area, T_∞ is the surrounding temperature (23 °C), ρ and V are the sample density and volume, respectively, and c is the heat capacity. The average value of c for steel between room temperature and 1000 °C is taken to be 691 J/kg K [52] and $\rho = 7800$ kg/m^3. Fitting the cooling data results in $h = 76$ W/m^{2}K, representing the combined effects of convection and radiation in the present experiments.

The effective convective heat transfer coefficient is used as a surface boundary condition for a transient heat conduction simulation using the finite element method with 1600 axisymmetric elements to simulate the sample. A constant body heat flux of 3.0×10^9 W/m^3 is used to simulate resistive heating based on estimates of the heat loss from the sample during steady-state heating at 1000 °C. The simulation uses temperature-dependent carbon steel properties gathered by Lee et al. [52] over the relevant temperature range. The contact conductance between the sample and the bars, h_{cond}, is assumed to be uniform, temperature-invariant and follow the definition given here:

$$\dot{Q}_{cond} = -h_{cond}A_s\left(T - T_{bar}\right) \tag{3}$$

Equation 3 gives the conductive heat flux from the sample to the bars through contact area A_s given the temperature difference across the interface given by T–T_{bar}. h_{cond} is determined by matching cooling data obtained from heat-only experiments where steel samples are heated using the same thermal profile used in the pulse-heated Kolsky bar experiments and are then allowed to cool within the bars. In the simulation, the full heating cycle on the specimen is simulated and heat is conducted into the bars to account for the temperature rise in both the sample and the bars on the heat flux during cooling. A value of $h_{cond} = 5500$ W/m^{2}K was found to match experiments between 700 and 750 °C for 1018 and 1075 steels, which covers most of the intercritical region, with the notable finding that the cooling rate did not depend on carbon content in the experiments. It was assumed that this conduction coefficient could be applied at all temperatures. This value is close to the result from an early analytical analysis of this heating method by Basak et al. [53].

Figure 6 shows the peak internal temperature gradients obtained from the simulations using the calibrated h_{cond} value as a function of temperature. The values are obtained from a single transient conduction simulation in which the sample temperature increases steadily up to about 1000 °C using a constant volume heat flux. The maximum axial temperature gradient increases steadily with apparent temperature. Apparent temperature is defined as the surface temperature in the middle of the sample and corresponds to the spot viewed by the pyrometer in the experiments. The peak temperature difference between the center and the edges of the specimen reaches 44 °C at an apparent temperature of 970 °C. The peak temperature occurs in the middle of the sample while the ends are cooler due to the heat flux into the bars. The largest axial gradients occur on the surface,

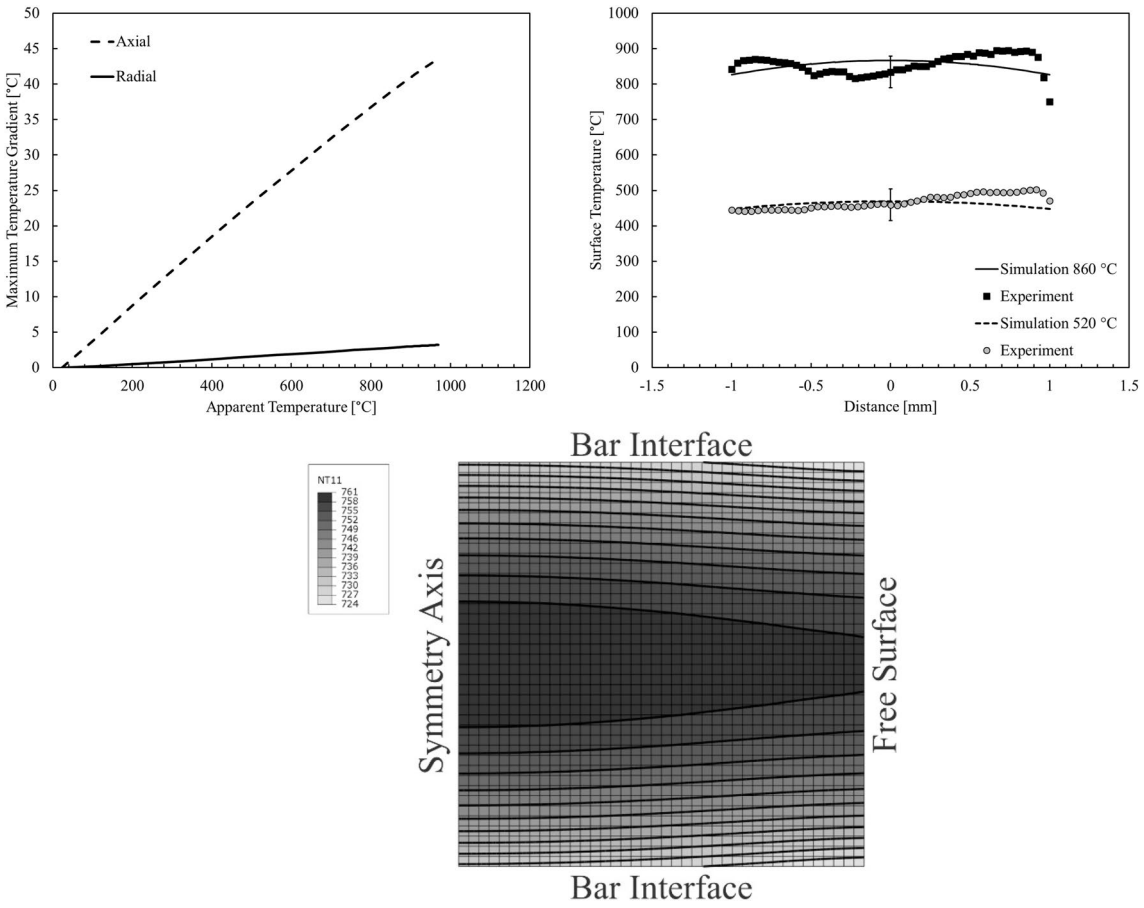

Fig. 6 Axial and radial peak temperature gradients (left) estimated from a finite element simulation of transient heating of a 1045 steel sample up to 1000 °C, and a comparison of the surface temperature distributions at two nominal test temperatures compared with thermal camera data (right). Uncertainty bars ($k=2$) on the thermal camera data apply to each data point and their origin is explained in [54]. Bottom: FEA-computed internal sample temperature distribution (NT11 = Temperature in °C)

although the axial gradients in the middle of the sample are only a few degrees lower. The computed maximum radial temperature gradient is much lower than the axial gradient, reaching only 5 °C at the maximum apparent temperature.

Although experimental corroboration of these internal thermal gradients is unavailable, previous work has shown that, when pearlite decomposition is interrupted in fast heating experiments, radial gradients exist in the quenched microstructure that support the existence of a radial temperature gradient [39]. Similar microstructural evidence is currently being developed to compare with the simulated axial thermal gradients. Measurements of the surface temperature distribution by infrared thermography are shown in Fig. 6 and compared to the simulated axial surface temperature distribution at two temperatures. The thermography data were obtained with a commercial infrared camera operating at 800 frames/s with a 25 µs integration time and a spatial resolution of 40 µm/pixel. The camera was calibrated with a blackbody furnace to 800 °C and assessed for uncertainties in a metal cutting application as described by Lane et al. [54]. The uncertainties relevant to the present application include those associated with calibration, wavelength and the point spread function of the optics. The experimental axial temperature gradients are of the same order as the simulation results, although the distribution is different. Figure 6 suggests the ends of the sample may be hotter than the middle rather than cooler as the simulations indicate, possibly due to the high resistance of the interfaces between the sample and foils, which is not captured in the model.

Taking into account the estimated internal thermal gradients from the finite element simulations, the experimental test temperatures and uncertainties are computed as follows:

$$T_{test} = \left(T_{TC} - \frac{\Delta T_{gradient}}{2}\right) \pm \left(\Delta T_{pyro} + \frac{\Delta T_{gradient}}{2}\right) \quad (4)$$

In Eq. 4, T_{TC} is the thermocouple temperature, $\Delta T_{gradient}$ is the axial internal temperature gradient and ΔT_{pyro} is the temperature difference between the control and monitoring pyrometers. This uncertainty includes both a random

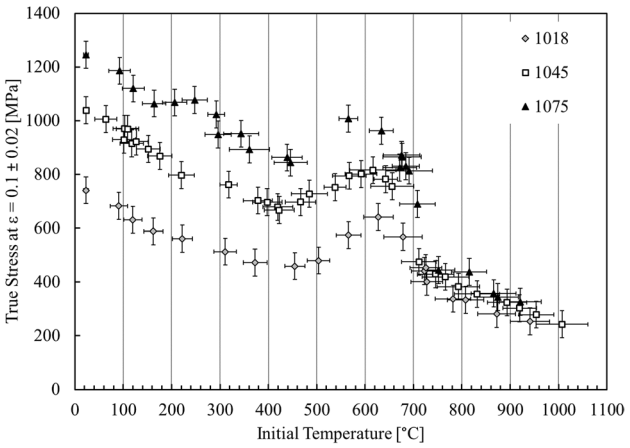

Fig. 7 Thermal softening behavior of three carbon steels at strain rates between 2000 to 5000 s^{-1} for a fixed true strain of 0.10 ± 0.02

component (the temperature uniformity, ΔT_{pyro}, that varies test-to-test) and a bias component ($\Delta T_{gradient}$). The uncertainty estimates for the pyrometer radiance temperature (±5 °C from reference [45] neglecting uniformity which is here accounted for by ΔT_{pyro}) and the thermocouple temperature (the greater of ±2.2 °C or ±0.75% [50]) are small compared to ΔT_{pyro} and $\Delta T_{gradient}$ and are hence neglected.

Finally, the uncertainty in the stress–strain data obtained using this technique is computed by error propagation methods assuming uncorrelated uncertainty components is estimated to be 20% on strain and 4% on stress. The uncertainty is exacerbated by the small size of the compression samples (4 mm diameter, or 27% of the bar diameter versus 80% suggested by Gray [55]) and by the presence of the graphite foils used to facilitate heating. The details of these uncertainty estimates are given elsewhere [49].

Results

Figure 7 presents the thermal softening behavior of the three carbon steels studied at a plastic strain of 0.1 between room temperature and 1000 °C. The three steels show very similar thermal softening patterns, with a prominent offset in the flow stress below A1 owing to differences in pearlite volume fraction (Table 2). The flow stress decreases approximately linearly from room temperature to about 400 °C, after which dynamic strain aging effects cause the flow stress to increase with further increases in temperature. The peak DSA stress seems to occur a bit below the A1 temperature. At A1, pearlite (cementite + ferrite) becomes unstable and dissolves to form austenite, causing the flow stress to drop sharply. The sharp drop is due to a combination of the disappearance of the hard cementite lamellae and, presumably, to the change in the nature of DSA hardening as BCC ferrite gives way to FCC austenite. This somewhat dramatic behavior at A1 is a consequence of the strain rates used in these tests: at lower rates, DSA hardening would have disappeared at temperatures well below A1 [24] and would not contribute to the sharp decline in flow stress seen in the present data set. Once the pearlite decomposes to austenite, which apparently happens very quickly (on the order of seconds), the flow stresses of the three steels are more comparable, demonstrating the greatly reduced effect of carbon as it transforms from a precipitate strengthener in BCC iron to an interstitial strengthener in FCC iron. Above A1, all three steels resume a gradual, approximately linear decrease in flow stress with slightly different slopes. At A3 and above all three steels exist in equilibrium as purely FCC austenite with different carbon contents. However, due to the short heating times used here, it is unlikely that any of the steels have reached uniform carbon distributions. The thermal softening behavior revealed in Fig. 7 naturally divides into four distinct regions: (1) the low temperature region (< 400 °C) showing nearly linear thermal softening followed by (2) the dynamic strain aging region where the flow stress increases with temperature, followed by (3) the pearlite decomposition region near A1, and finally (4) a second region of nearly linear thermal softening above A1. These regions will be discussed in turn. Before continuing, we note that descriptions of metal plasticity generally deal with the effects of temperature (as well as strain rate) on yield and strain hardening behavior separately. However, because the yield behavior is unknown in the present data set due to the finite plastic strain needed to develop stress equilibrium and strain rate uniformity, we are unable to uncouple the two. As such, we observe only the effect of temperature on plastic flow stress beyond the yield point.

Low Temperature Region (< 400 °C)

All three steels exhibit nearly linear thermal softening below 400 °C, indicating that carbon content (volume fraction of pearlite) does not strongly influence the thermal softening rate. Pearlite (cementite + ferrite) thus plays the role of an athermal, long-range barrier to slip in these materials at low temperature, as one would expect of large precipitates [20]. Below about 600 °C, the approximate minimum annealing temperature in carbon steels, the microstructure can be considered invariant, meaning that plasticity should be governed only by thermally-activated slip in BCC iron and there should be no thermal evolution of the microstructure or time-sensitive plasticity. That the three steels exhibit parallel thermal softening in this region confirms this view, and it points out that thermally-activated slip has a very similar nature in these steels regardless of the amount of pearlite present, up to nearly the eutectoid composition. Within pearlite, slip occurs in

the thin ferrite regions sandwiched between the cementite lamellae [56], although bending and fracture can occur in cementite plates themselves at large strains [57]. By contrast, slip in the globular ferrite grains does not have such a fine, imposed length scale, as the long range barriers, the grain boundaries, are much more widely spaced compared to the cementite lamellae. Thus, the data indicate that, despite the transition in the scale of the long-range barriers as slip transitions from grain-scale dominated to inter-lamellar-scale dominated as the pearlite fraction increases, the thermal sensitivity of flow stress does not change much. We note that Fig. 7 considers thermal softening at a single plastic strain level so hardening effects are masked. The evolution of hardening with temperature is examined later in the paper.

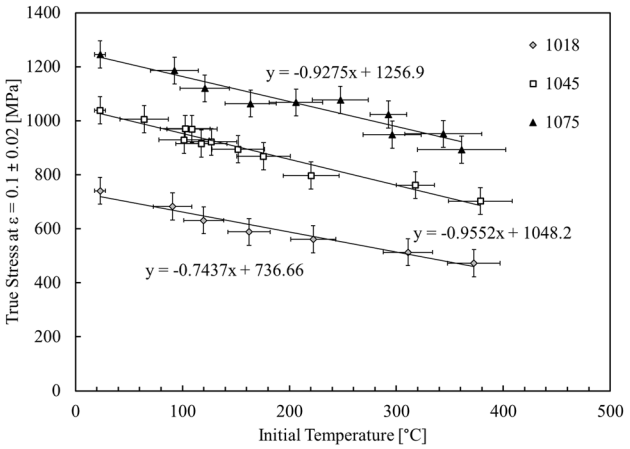

Fig. 8 Linear fits of thermal softening at a strain of 0.1 before the onset of dynamic strain aging

To compare the low present temperature thermal softening region with literature data, we fit the present data with the Johnson–Cook (JC) power law softening model [58]:

$$\frac{\sigma}{\sigma_0} = \left(1 - \left(\frac{T - T_{ref}}{T_{melt} - T_{ref}}\right)^m\right) \tag{5}$$

$$\sigma_0 = (A + B\epsilon^n)\left(1 + cln\left(\frac{\dot{\epsilon}}{\dot{\epsilon}_0}\right)\right) \tag{6}$$

In this model, σ is the flow stress, T is the temperature, T_{melt} is the alloy melting temperature, T_{ref} is room temperature (23 °C), ϵ is strain, $\dot{\epsilon}$ and $\dot{\epsilon_0}$ (= 1) are the strain rate and reference strain rate, respectively, and A, B, n, c and m are fitting coefficients. Values of the thermal softening parameter m were identified for the present three steels by fitting the stress–strain data (at all experimental plastic strains) up to the onset of DSA with the full JC model (Eqs. 5 and 6) using unconstrained optimization. For comparison, the absolute thermal softening rates, in terms of MPa/°C, are also determined over the same range by performing linear fits at fixed plastic strain (0.1), as shown in Fig. 8. The latter calculation is performed because m in the JC model yields relative, not absolute, thermal sensitivity, which can mask trends between steels of very different strength levels as illustrated below.

Table 4 Thermal softening fits from room temperature to below the onset of DSA compared to literature values for different carbon contents and strain rates

Material designation	m	$d\sigma/dT$ [MPa/°C]	T_{melt} (°C)	T_{ref} [°C]	Temperature range [°C]	Strain for fits	Strain rate [s^{-1}]	Ref
1018	0.60	− 0.74	1485*	23	23–400	0.1	3000	Present work
1045	0.75	− 0.96	1432*	23	23–400	0.1	3000	Present work
1075	0.94	− 0.93	1390*	23	23–400	0.1	3000	Present work
1012		− 0.54**			23–440	LYS	5000 (Region 2)	[15]
Armco Iron and 1006	1.0 (0.55)***	− 0.62**	1538	23	23–315**	0.1	2000**	[58]
1018	0.7**	− 0.66**	1427	23	23–300	0.1	1200	[59]
1016	0.65**	− 0.75**	1485**	23	23–400	0.1	450	[4]
1045	0.65**	− 1.20**	1432**	23	23–400	0.1	450	[4]
1045	1.0	− 0.92**	1460	23	23–600		7500	[18]
Various Structural Steels		− 0.00062 σ_y				LYS	< 0.000135	[60]

Certain commercial equipment, instruments, or materials are identified in this paper to specify the experimental procedure adequately. Such identification is not intended to imply recommendation or endorsement by the National Institute of Standards and Technology, nor is it intended to imply that the materials or equipment identified are necessarily the best available for the purpose

*Calculated with Thermocalc using the TCFE8 database

**Estimated by present authors using Eq. 5

***Value of m is 1.0 in [58], but this number is too low for the temperature range considered

The results of fitting the present data as well as available literature data up to 400 °C, along with the T_{melt} and T_{ref} values used for the JC fit, are shown in Table 4. The 1018 data show a similar m value but a higher absolute thermal sensitivity (in MPa/°C) compared to the results of Maekawa et al. [59], and those reported by Oxley [4], which are considered most comparable in terms of carbon content and deformation mode (compression). The results of Johnson and Cook [58] show a bit less thermal sensitivity (both absolute and m value), while the results of Campbell and Ferguson [15] show the lowest absolute thermal sensitivity. Regarding the Johnson and Cook [58] results, we note their m value for 1006 steel was likely influenced by thermal hardening caused by DSA, which is misleading here as we are concerned with temperature effects on slip without considering DSA. In fact, Johnson and Cook state explicitly that their $m = 1$ value for 1006 steel is influenced by the data above a homologous temperature of 0.2 (317 °C), which happens to be near where DSA effects being to appear at Kolsky bar strain rates. At lower temperatures they note that 1006 behaves more like pure iron ($m = 0.55$). The higher value of $m = 1$ is nevertheless listed in the paper as appropriate for 1006 steel. For the present comparison we therefore use $m = 0.55$ instead to represent their 1006 steel results and also to estimate the linear absolute thermal softening rate. With this adjustment, their results, on an absolute basis, are comparable to [59] though still slightly below the present results. The low carbon steel measurements of Campbell and Ferguson [15] show the lowest thermal sensitivity, a fact which may be attributed to their taking the lower yield stress values.

For the present medium carbon steel (1045), our results are quite comparable in absolute terms to those of Jaspers and Dautzenberg [18] but less thermally-sensitive than results reported in Oxley [4]. The $m = 1$ result reported for 1045 by Jaspers and Dautzenberg [18] is also, we feel, affected by DSA as their fit extends to 600 °C where DSA effects are obvious. We retain their original m value in Table 4 but use only data below 400 °C to calculate the absolute thermal softening rate. The data reported by Oxley [4] shows identical m values for 1045 and 1016 steels (as calculated by the present authors), but the absolute thermal softening rate for 1045 is much higher than for 1016 (also calculated here). This underscores the sometimes-confusing results when using m to determine the relative thermal sensitivity of different materials. For 1075 steel, the authors were unable to find appropriate literature data to compare the present results against.

From the foregoing comparisons, several general conclusions can be drawn. First, there is some scatter in the thermal softening rates obtained by different researchers for nominally the same steel, which is not unexpected given possible variation in alloying elements and material condition prior to testing. That said, the present results are generally comparable, in terms of thermal softening rates below 400 °C, under the rapid, direct-current heating used here compared to most other comparable measurements obtained under induction or furnace heating over usually longer heating timescales but with similar strain rates and carbon contents. This is as expected, given that time effects are unlikely in this low temperature region for such steels. Finally, although pearlite acts roughly as an athermal slip barrier, the thermal softening data seem to indicate a mild trend of increasing absolute thermal sensitivity with increasing carbon content. On closer examination of the high strain rate literature, this trend seems to hold as well. It is also apparent at low strain rate, according to a review of structural steel data by Seif et al. [60] at quasi-static strain rates ($< 0.000135\ s^{-1}$). They indicate the absolute thermal softening rate is directly proportional to the room temperature yield strength, as shown in Table 4. Room temperature yield strength is proportional to carbon content for the plain carbon steels examined here.

The apparent proportionality between strength (here, carbon content) and absolute thermal sensitivity cannot be explained within the framework of continuum plasticity theory that views cementite as a long-range barrier. The prime suspect for increasing thermal sensitivity with pearlite faction is scale effects on slip in BCC ferrite. As carbon content increases, plasticity transitions from slip mostly within ferrite grains measuring approximately 5 μm across to slip mostly within narrow interlamellar ferrite plates sandwiched by cementite with a thickness of about 0.2 μm. In BCC iron, reduction in grain size, a different long-range slip barrier, seems to have little effect on strain rate sensitivity (the usual analog to temperature sensitivity) for conventional grain size materials [61], and actually reduces rate sensitivity in nanocrystalline iron [62]. However, the increasing importance of geometrically necessary dislocations [63] generated at cementite-ferrite interfaces within pearlite [56] might be expected to influence plastic behavior with temperature in ways that may be different from ferrite grain boundaries. This likely means hardening behavior should change with pearlite fraction as well. This will be explored later in the paper.

Finally, Fig. 9 compares literature data on the effect of carbon content on flow stress for ferrite-pearlite steels under low strain rate deformation from McGannon [25] and Itabashi et al. [64] with the present data at room temperature and also tracks its evolution with temperature for the present data and those of Oxley [4] for high strain rates. The present high strain rate data indicate an 8% greater influence of carbon content using nominal compositions, rising to 20% greater using measured compositions (Table 1) compared to low strain rate room temperature data. We note the estimate from McGannon [25] is made with tensile strength data, and the result from Itabashi et al. [64] is computed from tensile

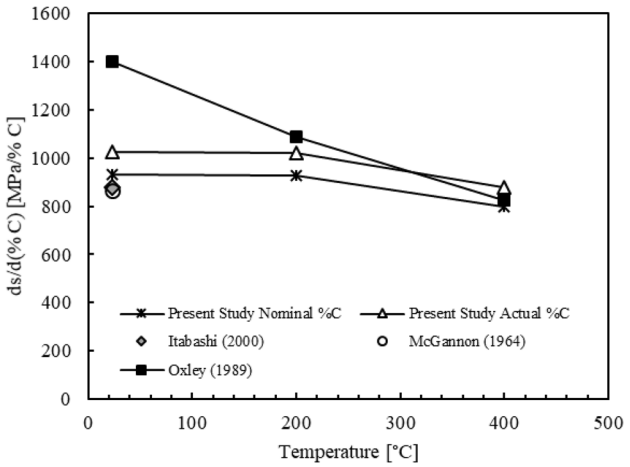

Fig. 9 Sensitivity of flow stress to carbon content at different temperatures of the present high strain rate data compared to literature sources

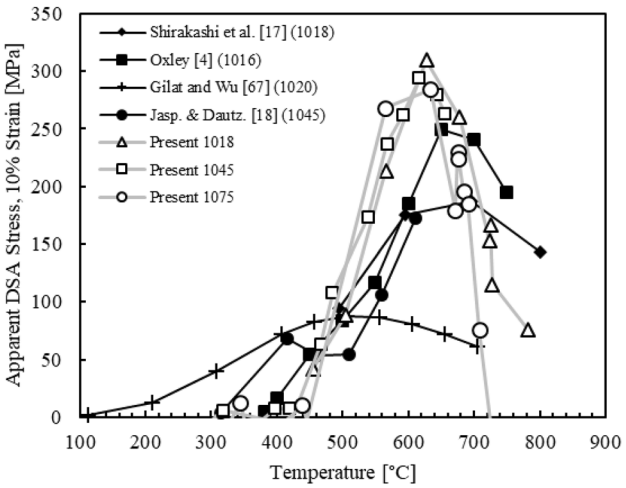

Fig. 10 Estimate of the DSA stress effect versus initial temperature

data at 0.1 strain. Increased sensitivity to carbon content may be due to deformation mode (tension vs. compression) or a strain rate effect, though the difference seems small considering the large effect that minor compositional variations has on the results. Thus the present data, in terms of the sensitivity of flow stress to carbon content at high strain rates, are generally in agreement with literature data at lower strain rates at room temperature.

Dynamic Strain Aging and Strain Hardening Evolution

Dynamic strain aging (DSA) in steels manifests itself in a variety of ways, including the upper and lower yield point behavior, "serrated" stress–strain curves, negative strain rate sensitivity owing to thermal hardening, and Portevin–Le Chatelier (PLC) effect [22, 24, 65]. Transmission electron microscopy (TEM) investigations suggest that DSA in BCC iron primarily involves carbon atoms pinning screw dislocations via a high temperature Peierls mechanism [66]. Under high strain rate loading conditions, phenomena such as PLC banding, which is highly transient on timescales of seconds or longer, are suppressed, but hardening effects due to more rapid dislocation accumulation remain. This gives rise to so-called negative strain rate sensitivity for particular combinations of temperature and strain rate.

As strain rate increases, the onset of DSA hardening is pushed to higher temperatures, as the diffusion of the relevant solute atmosphere must be able to catch up with dislocations in order to pin them. The onset temperature observed here, about 450 °C, is similar to what has been observed in carbon steels under high strain rate loading [4, 14, 18, 58]. Increasing strain rate has also been observed to reduce the DSA peak stress in carbon steel [23, 67]. The magnitudes of the stress increases owing to DSA are computed for the present steels by fitting the thermal softening data obtained at fixed plastic strain (e.g. Figure 7) up to the DSA onset temperature, then extrapolating the fit into the DSA region and subtracting the extrapolated stress from the observed stress. The fits were performed using the JC thermal softening model at 0.1 plastic strain. The results are shown in Fig. 10, along with similar estimates for comparable experiments from the literature computed by the authors using the same fitting method. While the onset temperatures observed here are quite comparable to the literature, the magnitudes of the peak DSA stresses are higher by 50 MPa or more, compared to literature sources. Of further note is that the stress magnitude does not seem to vary much with carbon content, in agreement with low strain rate tensile results [23]. The magnitude of the DSA stress effect is known to vary with alloy composition, particularly the amount of C, N, Mn and O, and with the amount of prior cold work and with grain size [24, 38]. In some cases, the stress magnitude can decrease with applied strain rate [67]. A clear difference between the present experiments and literature data, with the exception of [59], is the short heating times prior to deformation, which, for example, may tend to lessen any recovery that occurs in the microstructure, thereby potentially exacerbating the apparent DSA effects. However, the literature materials were either annealed or hot rolled, which limits the probability that significant recovery is possible due to the absence of cold work. The results of Gilat and Wu [67], which show very limited stress rise under torsion, may also indicate a dependence of DSA stress on deformation mode. Finally, we note that in all three steels, a peak occurs in the flow stress data somewhat below A1. Sub-critical annealing and spheroidization of the cementite plates will both tend to reduce the flow stress near A1, each according to different kinetic schedules. However, because of the limited heating

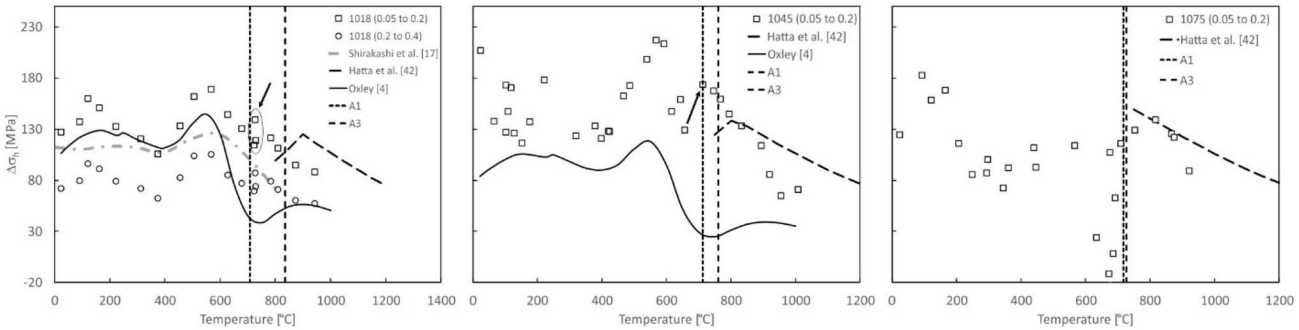

Fig. 11 Strain hardening versus temperature for the three steels and comparison to literature data. Circle and arrows indicate jump in hardening due to the formation of austenite above A1

times used in the present experiments, these effects may be quite limited compared to literature findings obtained under longer thermal soak times. Another possibility is a gradual reduction in the DSA stress brought about by the increasing mobility of solute atoms with increasing temperatures to the point where they no longer exert drag on dislocations [22].

The most important effect of dynamic strain aging regarding machining behavior is the increase in hardening rate that occurs for particular combinations of strain rate and temperature. The strain hardening evolution with temperature and carbon content is examined here by fitting each experimental stress–strain curve with a power law function (the Holloman equation) following the method of Oxley [4]:

$$\sigma = \sigma_1 \epsilon^n \tag{7}$$

Using the set of fit values of σ_1 and n, hardening is determined by computing the difference in flow stress between true strains of 0.05 and 0.20, which captures most of the data we have collected:

$$\Delta\sigma_h = \sigma_1(0.2^n - 0.05^n) \tag{8}$$

The variation of hardening with temperature and carbon content is shown in Fig. 11 and compared with literature data for similar steels and test conditions. Literature hardening values are computed between 0.2 and 0.4 plastic strain following the original sources. Hardening of the present 1018 data is also explored between 0.2 and 0.4 plastic strain because the data are available. As this plot shows, hardening decreases at higher plastic strains, which is of course expected for most metals. The hardening evolution of eutectoid steel with temperature is not readily available in the literature.

Figure 11 shows the evolution of the hardening behavior with carbon content. The 1018 and 1045 steels exhibit similar behavior, although the 1045 behavior is more ambiguous at lower temperatures. 1018 exhibits a fairly well defined, dual peak structure below A1, the second peak being associated with DSA. The 1045 steel also shows a prominent second peak in the DSA region, but at lower temperatures the hardening trend is not as clear. 1075 hardening in the DSA region is quite different, showing a sharp minimum just below A1. All three steels show an increase in hardening near A1, indicated by arrows in the 1018 and 1045 plots, due to the formation of FCC iron via phase transformation. Beyond A1, all three steels show a gradual decline in hardening with further increases in temperature. The 1075 steel shows the largest increase in hardening at A1, which is enhanced by a steep decline in hardening to essentially zero just below A1. Full stress strain curves in this hardening transition region are shown in Fig. 12 for the 1075 steel. After the sharp minimum in hardening below A1, the hardening increases dramatically before following a gradual decline with further increases in temperature, similar to the other two steels. We note that classical plasticity considers

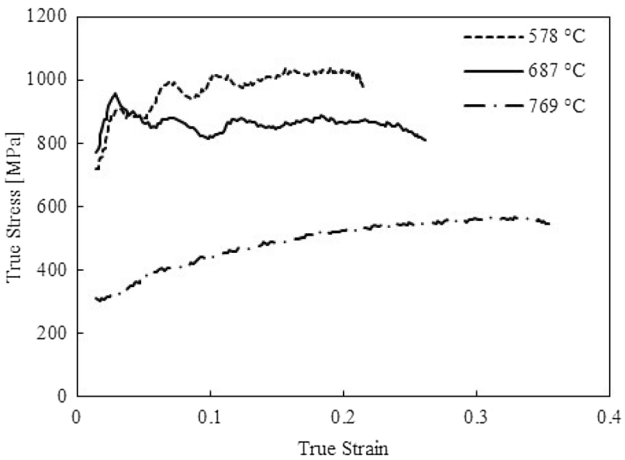

Fig. 12 Dynamic stress–strain curves of 1075 steel near the A1 temperature showing a transition from peak hardening to near zero hardening close to A1, followed by a large increase in hardening rate beyond A3 indicative of dynamic strain aging giving way to phase transformation

BCC hardening to be temperature-independent at low temperatures, in contrast to FCC hardening [68]. The 1018 steel hardening is roughly temperature independent below the DSA range, but for higher carbon contents, it is less so.

Literature hardening data determined from the Oxley fits of Oyane et al. [16] and from the data of Maekawa et al. [59] have a similar character for both 1018 and 1045 steels up to and including the peak hardening in the DSA region. The magnitudes of the hardening levels are fairly similar to the present 1018 measurements but for 1045 the present data indicate significantly higher hardening. Near A1, however, the Oxley [4] hardening pattern diverges from the present data, exhibiting a very low hardening rate at A1, followed by a gradual increase through the intercritical region and, in the case of 1018, a mild reduction towards 1000 °C. The magnitude of the hardening loss from the DSA peak to the trough near A1 is about 100 MPa, which is on the order of the drop seen in the present 1045 data but significantly higher than what is observed in the 1018 data. The Maekawa et al. [59] hardening rate drops more gradually up to A1, but the hardening does not increase through the intercritical range as anticipated, perhaps because the data were limited in temperature to 800 °C. The magnitudes of the hardening for the present 1018 steel between 0.2 and 0.4 plastic strain are lower by about 50 MPa than both literature data below A1, but actually exceed the literature data above A1. Hardening is much higher in the present 1045 data below A1 because it is computed at lower strain levels than the literature data, and extrapolations of the present data were not attempted. Overall, below A1 the present hardening results are in qualitative accord with comparable literature data.

Above A1, where pearlite is partially or completely dissolved and the microstructures consist of BCC ferrite and FCC austenite, the hardening evolution with temperature is simpler than it is below A1. We compare the present data with the model by Hatta et al. [42], which is valid for carbon steels of varying carbon content above the A1 temperature and for strain rates up to 100 s^{-1}. For comparison purposes this model is extrapolated to a strain rate of 3000 s^{-1} using the Zener-Holloman rate sensitivity included in the model, and stress–strain curves are generated for each steel composition examined up to 1200 °C. The hardening behavior is evaluated using Eq. 8. We further assume that adiabatic heating effects in this model are embedded in the fit parameters. The model indicates the hardening falls monotonically with temperature after peaking at A3. We note that the A3 values in the Hatta model differ from those calculated here, which include contributions from other alloying elements besides carbon. The poorest agreement is with the 1018 data, where the measured hardening falls below the Hatta model prediction, which may indicate that the present results have a smaller portion of FCC austenite compared to their data due to short heating times and limited carbon diffusion. For the other two steels, the agreement is fairly good, although in the case of 1045 steel the hardening declines more quickly with temperature compared to the model. It was anticipated that the best agreement would be with 1075 steel due to the small amount of globular ferrite in the microstructure which facilitates more rapid carbon homogenization of the austenite. The hardening comparison tends to bear this out. Further comparisons between this model and the flow stress evolution with temperature are described later. Overall, it is clear from Fig. 11 that steel hardening behavior with temperature behaves differently depending on the amount of pearlite in the microstructure. The difference is most pronounced near A1, but even at lower temperatures there are significant differences. This behavior may be associated with differences in how dislocation generation and accumulation occur during deformation within interlamellar ferrite inside pearlite versus within globular ferrite grains.

Behavior Near A1

Near A1, the flow stress of all three steels undergoes a dramatic change as the pearlite dissolves into austenite. Under rapid heating, the transformation may be incomplete, and when the sample is trapped and quenched between the bars (500 °C/s cooling rate or more) after compression, regions that have transformed to austenite will, depending on the carbon concentration, form martensite, bainite, or other quenched phases. Because these microconstituents do not exist in the starting steels, their presence in the tested samples is indicative of transformation. Previous work on these steels has suggested that pearlite dissolves in under three seconds [39], but it was also shown that the transformation occurs non-uniformly through the volume of the sample due to the radial and axial temperature gradients that exist in the samples as described earlier. Because of the non-uniformity of the microstructures, it is impossible to precisely measure the extent of the transformation from a single micrograph; the entire sample needs to be interrogated. Instead, we here present only examples of the quenched results of partial transformations above A1 for the three steels examined. Austenite forms first within pearlite colonies, growing from the ends of cementite lamellae and eventually consuming the colony. Within the intercritical region, given enough heating time, equilibrium fractions of high carbon austenite and low carbon ferrite should exist in the microstructure with homogenous carbon distributions in each phase. Figure 13 shows evidence of transformed regions near A1 for all three steels where the microconstituents are resolved with LePera's etch [69] and imaged using a scanning electron microscope (SEM). Martensite is only lightly etched

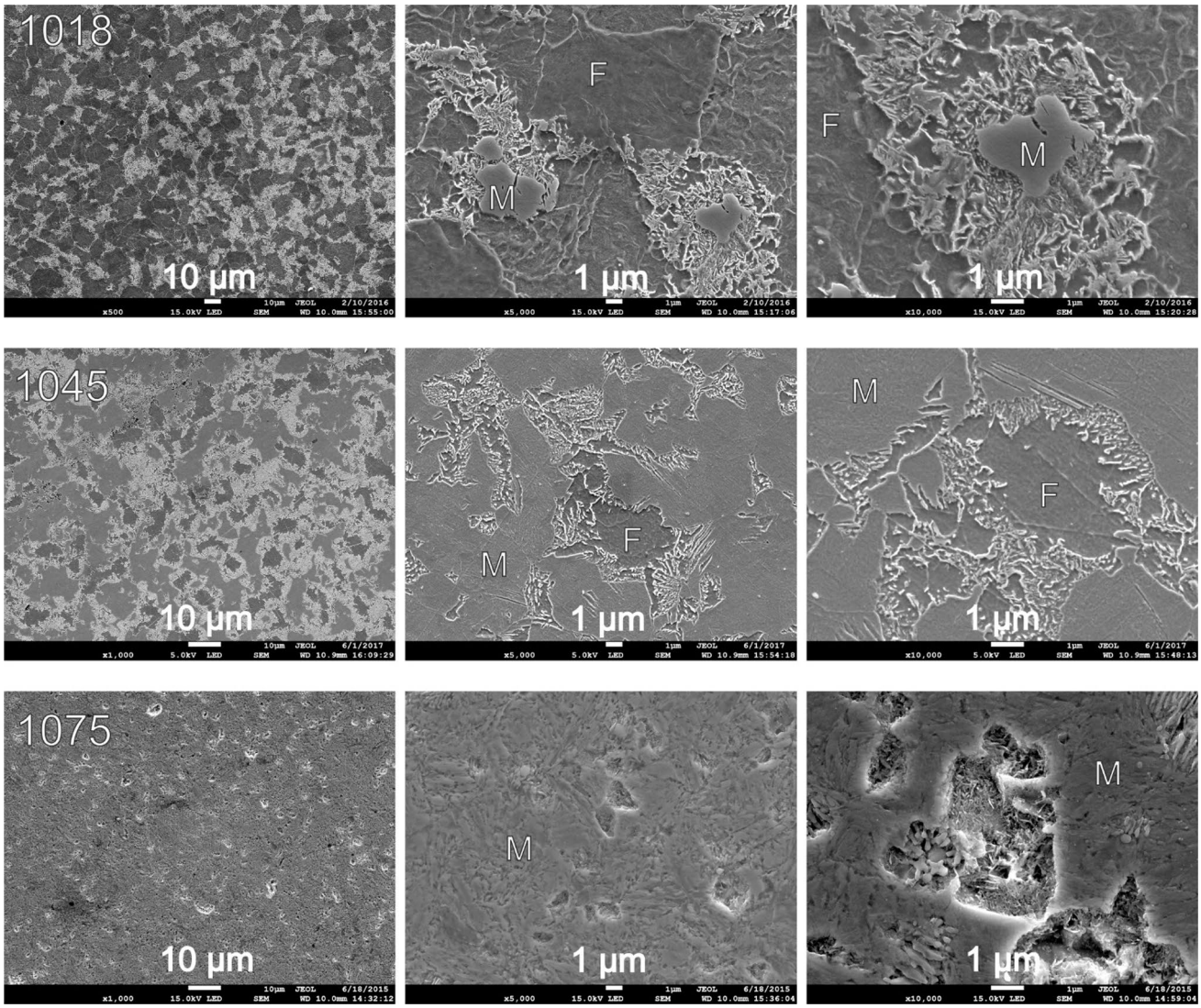

Fig. 13 SEM images of tested and quenched samples just above A1 for the following conditions (top) 1018, 725 °C ± 33 °C, La Pera's etch; (middle) 1045, 711 °C ± 36 °C, La Pera's etch; (bottom) 1075, 708 °C ± 37 °C, nital etch. M: martensite. F: ferrite

and thus appears relatively featureless. These martensitic regions are usually surrounded by what appears to be a form of bainite and are of a lighter shade compared to the darker ferrite regions. Ferrite, being much softer than martensite, often shows polishing scratches and perhaps evidence of plastic strain. Some ferrite-ferrite grain boundaries are also evident. The irregular cementite particles surrounding martensite, probably also a form of bainite, stand in stark contrast to the parallel cementite lamellae of the original pearlite (Fig. 1). Retained pearlite does not appear in the selected micrographs of Fig. 13, but it was observed elsewhere in the microstructures and occurs more readily in lower-temperature regions. Little or no ferrite is found in the 1075 samples heated to 726 °C (A3 = 727 °C). Instead only small, spheroidal pockets of needle-like cementite particles, appearing in the bottom of Fig. 13, probably another form of bainite, result from incomplete diffusion of carbon into original ferrite grains during the short heating process.

We note, in reference to Fig. 7, how the microstructural changes observed near A1 are associated with a large and fairly sudden drop in the flow stress in all three steels. Certainly, the loss of hard cementite particles contributes to the strength loss. However, an important component must also be the disappearance of dislocation pinning by solute atmospheres associated with dynamic strain aging, since it is assumed that this effect is responsible for the pronounced strengthening in the DSA region leading up to A1. While DSA effects have been observed in FCC steels, owing to substitutional solute atmospheres, the effects are limited to serrated flow rather than a strong increase in hardening

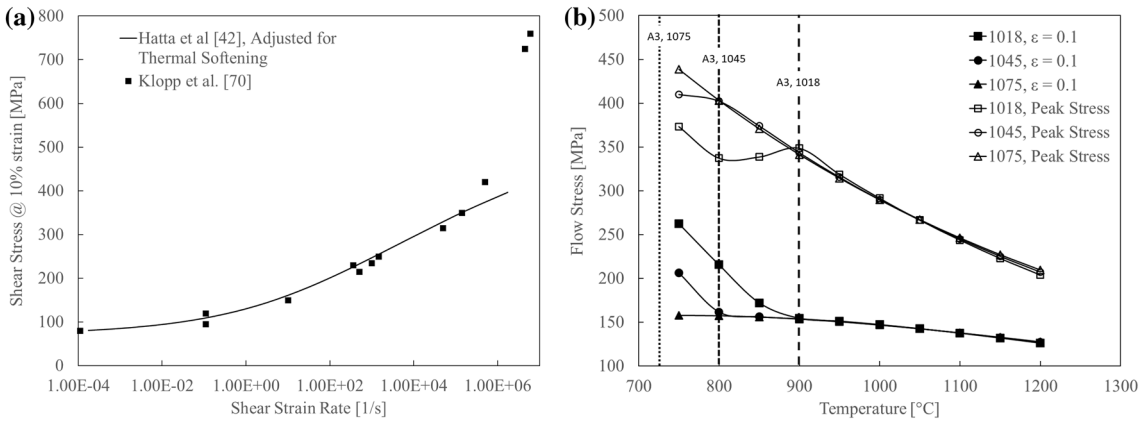

Fig. 14 Strain rate sensitivity (**a**) and flow stress vs. temperature at 0.1 plastic strain and peak flow stress (**b**) predicted by the Hatta et al. model [42] for the present steels and for the room temperature pure iron data from reference [70]

rates seen in BCC steels [22]. Thus it seems the rapid disappearance of BCC ferrite during austenite formation tends to eliminate much of the strengthening associated with solute pinning of dislocations, adding to the overall loss in flow stress above A1. It is remarkable that the flow stress of 1018 steel also drops rather rapidly near A1 even though this steel contains much more globular BCC ferrite than the other steels, and it persists until the much higher A3 temperature. One possibility is that DSA strengthening is associated primarily with interlamellar BCC inside pearlite colonies and is less potent within the globular ferrite, and since the pearlite disappears rather suddenly past A1, most of the DSA effects disappear suddenly as well. Regardless, that the dramatic change in flow stress near A1 may have as much or more to do with the disappearance of DSA than with the dissolution of pearlite has a very important implication on steel behavior in machining, for two reasons. First, short heating times may exacerbate the effect of DSA on flow stress by limiting the amount of recovery that can take place and/or inhibiting carbide coarsening which may also alter the effects associated with DSA. Second, it is known that the onset temperature for DSA increases with strain rate, but the A1 temperature, where DSA effects seem to disappear, is thermodynamically fixed. Thus, if very high cutting velocities are used, the strain rate may be pushed so high that the onset temperature for DSA may be pushed beyond A1 and perhaps these effects may be bypassed altogether. On the other hand, as cutting velocities increase, transformation is inhibited by the limited time available for diffusion. The behavior near A1 during machining is indeed quite complex and time-dependent and may depend greatly on the cutting conditions.

Post-A1 Behavior

In the intercritical regime between A1 and A3, carbon steels exist as a mixture of high carbon FCC and low-carbon BCC, with phase fractions approaching those given by equilibrium phase diagram over prolonged times. Above A3 (Table 2), the steels are entirely FCC, until about 1390 °C iron may transform again to BCC (δ-iron) depending on carbon content [25]. Equilibrium distributions of FCC and BCC within the A1 to A3 region are achieved when carbon is given enough time to diffuse over length scales that are much larger than the inter-lamellar spacing of the original pearlite [29]. As shown earlier in Table 2, while A1 changes slightly with carbon content, A3 increases significantly as carbon levels are reduced. For example, 1018 steel remains, over long time scales, a ferrite/austenite mixture until 836 °C, whereas 1075 steel is expected to be completely austenitic at 727 °C. Thus in the present experiments, within the A1 to A3 region, the rapidly-heated steels examined here are expected to contain less FCC and more BCC compared to equilibrium due to the short heating times used, which informs expectations for the flow stresses observed in these experiments compared to comparable data in the literature for longer heating times.

To explore how the present results deviate from equilibrium behavior, we again invoke the model of Hatta et al. [42] which describes steel strength above A1 as a function of carbon content and temperature for strain rates up to 100 s^{-1}. The model uses a Zener–Holloman relationship for strain rate sensitivity, which adequately captures the behavior of pure iron (BCC) up to about 10^4 s^{-1} at low temperatures, where thermally-activated slip remains a dominant deformation mechanism. This is shown in Fig. 14a, which compares flow stress-vs-strain rate of pure iron computed by the Hatta et al. model at 800 °C with room temperature iron data over a wide range of strain rates up to 10^7 s^{-1} [70]. An 80 MPa offset was applied to the model prediction to adjust for the difference in strength between the high temperature steel model and the room temperature iron data. The model follows the data up to a shear strain rate of about 100,000 s^{-1}

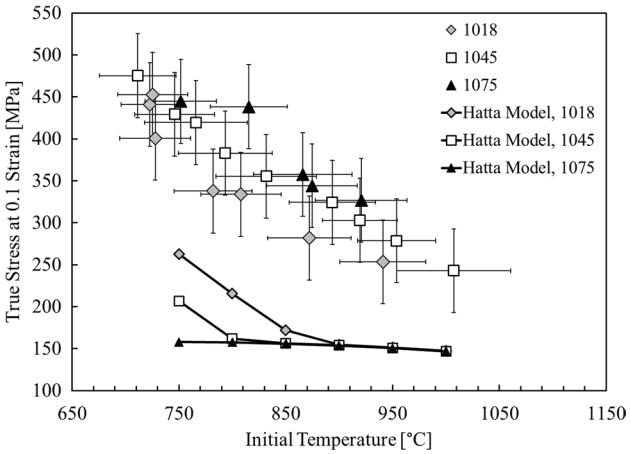

Fig. 15 Thermal softening behavior of rapidly heated steels above A1 compared to Hatta et al. model predictions [42]

(normal strain rate of 58,000 s^{-1}), so its use here to compare with the present data at 3000 s^{-1} seems justifiable. We note that in the Hatta et al. model the rate sensitivity of FCC iron is different, but relevant data are not readily available to check the model over the relevant range of strain rates. We further note that at high temperatures and low strain rates, creep is the dominant deformation mechanism, and steels in this regime generally show much larger strain rate sensitivities and lower deformation stresses [71].

In Fig. 14b, the Hatta et al. model is used to calculate the flow stress at 0.1 plastic strain for the present steel compositions as well as the peak stress, which is the stress at which hardening saturates and strain softening begins. Two important features stand out regarding the predicted equilibrium thermal softening behavior of steels above A1 predicted by this model. First, below A3, carbon content is negatively correlated to flow stress at low plastic strains because more carbon means more equilibrium FCC austenite in the microstructure, which is weaker than BCC ferrite. The peak stress, which occurs generally above 0.2 plastic strain, remains positively correlated with carbon content however, owing to the larger strain hardening capacity of the FCC austenite. Second, beyond the highest A3 temperature (for 1018 steel), where all three alloys exist as single-phase FCC but with different carbon levels, the model predicts no influence of carbon content on flow stress. The present data are compared to the Hatta et al. model prediction in Fig. 15. The rapidly-heated measurements show little evidence of BCC strengthening in the intercritical region. Instead, carbon content continues to have a positive correlation to flow stress over the entire range of temperatures examined at low plastic strain.

That there is no inversion of the flow stress dependence on carbon in this region is curious since 1018 should have more BCC ferrite and less FCC austenite compared to equilibrium conditions, given the short heating times. The 1018 should also have more ferrite than the 1075 steel for the whole 1018 intercritical range. Ferrite, according to the model, is stronger than austenite at low plastic strains, so the ferrite present in the 1018 intercritical region should produce a stronger response compared to 1075 at an equivalent temperature, as shown in the model. The effects of short heating times on the microstructure are varied. First, short heating times will tend to limit the carbon content of BCC below A1 compared to usual behavior (carbon content in BCC increases slightly up to A1), making post-A1 BCC carbon-deficient in these experiments, which would tend to reduce interstitial strengthening. Grain growth effects, which are embedded in the experimental data upon which the Hatta model is built, may tend to alter the relative strengths of FCC and BCC if the grain growth rates are different. That the present data are several hundred MPa stronger than the Hatta model suggests grain growth is restricted significantly by rapid heating, although this has yet to be investigated microstructurally. Higher carbon levels in austenite can enhance grain growth given sufficient time [72], which will also tend to weaken higher carbon steel at low strains compared to lower carbon steel in the austenite region. Here, this effect is also likely suppressed due to rapid heating. It could also be that the Hatta model under-predicts the rate sensitivity of the steel in this region, which is suggested by an examination of the comparison of the Hatta model with the data in their original paper. These sources, and perhaps others, must be investigated further, and the results used to inform kinetics-based models for the flow stress behavior of carbon steels near A1 under rapid heating conditions.

Conclusions

The following conclusions are drawn from the present investigation of the dynamic flow stress of carbon steels under short heating times using the NIST pulse heated Kolsky bar:

1 The thermal softening rates observed at high strain rates but below the onset temperature for dynamic strain aging effects are similar to literature values obtained over wide ranges of strain rates and carbon contents. Thermal softening does not depend strongly on pearlite content, in accord with the athermal role of cementite in carbon steel plasticity. However, a weak dependence of absolute thermal softening rates on carbon content exists and it is consistent with literature data at low strain rates. This dependence may be related to the reduction in the available slip length as the dominant plastic deformation process transitions from globular ferrite in low carbon steel (5 μm grain size) to inter-lamellar ferrite in high carbon steel (0.2 μm plate thickness).

2 Hardening behavior, for plastic strains less than 0.20, changes with pearlite fraction, going from weak to strong temperature dependence, and including a sharp minimum of near zero hardening near A1 for the highest carbon steel.
3 The magnitude of the peak stress in the dynamic strain aging region is not strongly dependent on carbon content and the present measurements show stronger peak stresses here compared to comparable data in the literature.
4 The dramatic change in flow stress near A1 is due to a combination of dissolving cementite particles within pearlite colonies and the disappearance of increased hardening rates associated with dynamic strain aging as the pearlite colonies transform rapidly to austenite.
5 Given that the dynamic strain aging onset temperature increases with strain rate but the effect disappears at the thermodynamically-fixed A1 temperature, it is possible that for very rapid machining processes (high speed machining) where the strain rates are much higher than Kolsky bar rates (10^6 versus 10^3 s^{-1}), large excursions in flow stress due to DSA observed here may be significantly modifed. The reduced time for phase transformation at high cutting speeds further complicates the picture near A1.
6 Carbon maintains a positive role on flow stress above A1 as an interstitial in FCC iron, which runs counter to the expected behavior. Explanations for this are varied but are likely also related to very short heating times.

Acknowledgements The authors gratefully acknowledge the efforts, support and input of the following individuals in the experimental work underpinning this paper: Debasis Basak, Tim Burns, Matt Davies, Richard Fields, Sindhura Gangireddy, Lyle Levine, Eric Whitenton, Maureen Williams, Howard Yoon and Sandra Young at NIST and Eli Marcus of the Nuclear Research Center Negev, Israel.

References

1. Tlusty J (2000) Manufacturing processes and equipment. Prentice-Hall, Upper Saddle River
2. Trent EM, Wright PK (2000) Metal cutting. Butterworth-Heinemann, Boston
3. Arrazola PJ et al (2013) Recent advances in modelling of metal machining processes. CIRP Ann Manuf Technol 62:695–718
4. Oxley PLB (1989) Mechanics of machining: an analytical approach to assessing machinability. Wiley, New York
5. Özel T, Altan T (2000) Determination of workpiece flow stress and friction at the chip-tool contact for high-speed cutting. Int J Mach Tools Manuf 40:133–152
6. Shatla M, Kerk C, Altan T (2001) Process modeling in machining. Part I: determination of flow stress data. Int J Mach Tools Manuf 41:1511–1534
7. Warnecke G, Oh J-D (2002) A new thermo-viscoplastic material model for finite-element-analysis of the chip formation process. CIRP Ann Manuf Technol 51(1):79–82
8. Özel T, Zeren E (2006) A methodology to determine work material flow stress and tool-chip interfacial friction properties by using analysis of machining. ASME J Manuf Sci Eng 128:119–129
9. Shrot A, Bäker M (2012) Determination of Johnson-Cook parameters from machining simulations. Comput Mater Sci 52:298–304
10. Dirikolu MH, Childs THC, Maekawa K (2001) Finite element simulation of chip flow in metal machining. Int J Mech Sci 43:2699–2713
11. Schulze V et al (2011) Modeling the process-induced modifications of the microstructure of work piece surface zones in cutting processes. Adv Mater Res 223:371–380
12. Han A et al (2008) White layer formation due to phase transformation in orthogonal machining of AISI 1045 annealed steel. Mater Sci Eng A 488:195–204
13. Duan CZ, Zhang LC (2012) Adiabatic shear banding in AISI 1045 steel during high speed machining: mechanisms of microstructural evolution. Mater Sci Eng A 532:111–119
14. Manjoine MJ (1944) Influence of rate of strain and temperature on yield stresses of mild steel. J Appl Mech 11:A211–A218
15. Campbell JD, Ferguson WG (1970) The temperature and strain-rate dependence of the shear strength of mild steel. Philos Mag 21:63–81
16. Oyane M et al (1967) The behaviour of some steels under dynamic compression. In 10th Japan Congress on Testing Materials
17. Shirakashi T, Maekawa K, Usui E (1983) Flow stress of low carbon steel at high temperature and strain rate (Part 1)—propriety of incremental strain method in impact compression test with rapid heating and cooling systems. Bull Japan Soc Prec Eng 17(3):161–166
18. Jaspers SPFC, Dautzenberg JH (2002) Material behavior in conditions similar to metal cutting: flow stress in the primary shear zone. J Mater Process Technol 122:322–330
19. Lee W-S, Liu C-Y (2006) The effects of temperature and strain rate on the dynamic flow behavior of different steels. Mater Sci Eng A 426:101–113
20. Follansbee PS (2014) Fundamentals of strength. Wiley, New York
21. Cottrell AH, Bilby BA (1949) Dislocation theory of yielding and strain ageing of iron. Proc Phys Soc A 62(49):49–62
22. Baird JD (1973) In The inhomogeneity of plastic deformation. American Society for Metals, Metals Park, pp 191–220
23. Li C-C, Leslie WC (1978) Effects of dynamic strain aging on the subsequent mechanical properties of carbon steels. Metall Trans A 9A:1765–1775
24. Robinson JM, Shaw MP (1994) Microstructural and mechanical influences on dynamic strain aging phenomena. Int Mater Rev 39(3):113–122
25. McGannon HE (1964) The making, shaping and treating of steel, 8th ed. US Steel, Pittsburg
26. Sachdev AK (1982) Dynamic strain aging of various steels. Metall Trans A 13A:1793–1797
27. Cady CM et al (2000) Dynamic materials testing, texture, and yield-surface calculation of an automotive sheet steel. Metall Mater Trans A 31A:2439–2448
28. Rodriguez P (1984) Serrated plastic flow. Bull Mater Sci 6(4):653–663
29. Speich GR, Demarest VA, Miller RL (1981) Formation of austenite during intercritical annealing of dual-phase steels. Metall Trans A 12A:1419–1428
30. Datta DP, Gokhale AM (1981) Austenitization kinetics of pearlite and ferrite aggregates in a low carbon steel containing 0.15 Wt Pct C. Metall Trans A 12A:443–450

31. Esin VA et al (2014) Situ synchotron X-ray diffraction and dilatometric study of austenite formation in a multi-component steel: influence of initial microstructure and heating rate. Acta Mater 80:118–131
32. Ashby MF, Easterling KE (1984) The transformation hardening of steel surfaces by laser beams-I. Hypo-eutectoid steels. Acta Metall 32(11):1935–1948
33. Caballero FG, Capdevila C, García de Andrés C (2001) Modelling of isothermal formation of pearlite and subsequent reaustenitisation in eutectoid steel during continuous heating. Mater Sci Technol 17:686–692
34. Roósz A, Gácsi Z, Fuchs EG (1983) Isothermal formation of austenite in eutectoid plain carbon steel. Acta Metall 31(4):509–517
35. Roberts GA, Mehl RF (1943) The mechanism and the rate of formation of austenite from ferrite-cementite aggregates. Trans Am Soc Met 31:613
36. Atkinson C, Akbay T, Reed AC (1995) Theory for reaustenitisation from ferrite/cementite mixtures in Fe-C-X steels. Acta Metall Mater 43(5):2013–2031
37. Kaluba WJ, Taillard R, Foct J (1998) The bainitic method of austenite formation during rapid heating. Acta Mater 46(16):5917–5927
38. Castro Cerda FM et al (2017) Austenite formation in 0.2% C and 0.45% C steels under conventional and ultrafast heating. Mater Des 116:448–460
39. Mates SP, Stoudt M, Gangireddy S (2016) Measuring the influence of pearlite dissolution on the transient dynamic strength of rapidly heated plain carbon steels. J Met 68(7):1832–1838
40. Semiatin SL et al (2017) The radial temperature gradient in the gleeble hot torson test and its effect on the interpretation of plastic flow behavior. Metall Mater Trans A 48A:5357–5367
41. Davis JR (eds.) (1998) Metals handbook. ASM International, Materials Park
42. Hatta N et al (1985) Modelling on flow stress of plain carbon steel at elevated temperatures. Steel Res 56(11):575–582
43. Panigrahi BK (2001) Processing of low carbon steel plate and hot strip—an overview. Bull Mater Sci 24(4):361–371
44. Martínez-de-Guerenu A et al (2004) Recovery during annealing in a cold rolled low carbon steel. Part I: kinetics and microstructural characterization. Acta Mater 52:3657–3664
45. Mates SP, Rhorer R, Whitenton E, Burns T, Basak D (2008) A pulse-heated kolsky bar technique for measuring the flow stress of metals at high loading and heating rates. Exp Mech 48:799–807
46. Kinsey B et al (2013) Investigation of electroplastic effect at high deformation rates for 304SS and Ti-6Al-4V. CIRP Ann Manuf Technol 62:279–282
47. Okazaki K, Kagawa M, Conrad H (1980) An evaluation of the contributions of skin, pinch and heating effects to the electroplastic effect in titanium. Mater Sci Eng 45:109–116
48. Safa K, Gary G (2010) Displacement correction for punching at a dynamically loaded bar end. Int J Impact Eng 37(4):371–381
49. Gangireddy S, Mates SP (2017) High temperature dynamic response of a Ti-6Al-4V alloy: a modified constitutive model for gradual phase transformation. J Dyn Behav Mater 3(4):557–574
50. ASTM International (1993) Manual on the use of thermocouples in temperature measurement
51. DeWitt DP, Incropera FP (1988) Physics of thermal radiation. In Theory and practice of radiation thermometry. Wiley, New York
52. Lee S-J, Pavlina EJ, Van Tyne CJ (2010) Kinetics modeling of austenite decomposition for an end-quenched 1045 steel. Mater Sci Eng A 527:3186–3194
53. Basak D et al (2004) Temperature control of pulse heated specimens in a kolsky bar apparatus using microsecond time-resolved pyrometry. Int J Thermophys 25(2):561–574
54. Lane B et al (2013) Uncertainty of temperature measurements by infrared thermography for metal cutting applications. Metrologia 50:637–653
55. Gray GT (1990) Classic split-hopkinson pressure bar testing. ASM International, Materials Park
56. Dollar M, Bernstein IM, Thompson AW (1988) Influence of deformation substructure on flow and fracture of fully pearlitic steel. Acta Metall 36(2):311–320
57. Langford G (1977) Deformation of pearlite. Metall Trans A 8A:861–875
58. Johnson GR, Cook WH (1983) A constitutive model and data for metals subjected to large strains, high strain rate, and temperatures. In International Symposium on Ballistics, The Hague
59. Maekawa K, Shirakashi T, Usui E (1983) Flow stress of low carbon steel at high temperature and strain rate (Part 2)—flow stress under variable temperature and variable strain rate. Bull Japan Soc Prec Eng 17(3):167–172
60. Seif M et al (2016) Temperature-dependent material modeling for structural steels: formulation and application. National Institute of Standards and Technology, Gaithersburg
61. Harding J (1969) The effect of grain size and strain rate on the lower yield stress of pure iron at 288 K. Acta Metall 17:949–958
62. Jia D, Ramesh KT, Ma E (2003) Effects of nanocrystalline and ultrafine grain sizes on constitutive behavior and shear bands in iron. Acta Mater 51:3495–3509
63. Ashby MF (1970) The deformation of plastically non-homogeneous materials. Philos Mag 21:399–424
64. Itabashi M, Kawata K (2000) Carbon content effect on high-strain-rate tensile properties for carbon steels. Int J Impact Eng 24:117–131
65. Van Den Beukel A, Kocks UF (1982) The strain dependence of static and dynamic strain-aging. Acta Metall 30:1027–1034
66. Caillard D, Bonneville J (2015) Dynamic strain aging caused by a new Pierels mechanism at high-temperature in iron. Scripta Mater 95:15–18
67. Gilat A, Wu X (1997) Plastic deformation of 1020 steel over a wide range of strain rates and temperatures. Int J Plast 13(6–7):611–632
68. Zerilli FJ, Armstrong RW (1987) Dislocation-mechanics-based constitutive relations for material dynamics calculations. J Appl Phys 61(5):1816–1825
69. LePera FS (1979) Improved etching technique for the determination of percent martensite in high-strength dual-phase steels. Metallography 12:263–268
70. Klopp RW, Clifton RJ, Shawki TG (1985) Pressure-shear impact and the dynamic viscoplastic response of metals. Mech Mater 4:375–385
71. Frost HJ, Ashby MF (1982) Deformation-mechanism maps: the plasticity and creep of metals and ceramics. Pergammon Press, New York
72. Wray PJ (1982) Effect of carbon content on the plastic flow of plain carbon steels at elevated temperatures. Metall Trans A 13A:125–134